

Investigation of Mold Flux Entrainment in CC Molds Due to Shear Layer Instability

Lance C. Hibbeler and Brian G. Thomas
University of Illinois at Urbana-Champaign
Department of Mechanical Science and Engineering
1206 West Green Street, MC-244
Tel.: +1-217-333-6919
Fax: +1-217-244-6534
Email: lhibbel2@illinois.edu, bgthomas@illinois.edu

Key words: Mold Flux Entrainment, Kelvin-Helmholtz Instability, Inclusions, Continuous Casting, Computational Fluid Dynamics

ABSTRACT

Mechanisms for mold flux entrainment in continuous casting molds include vortexing and suction down the SEN due to asymmetric fluid flow, excessive upward flow impingement on the meniscus, surface level fluctuations, argon bubble effects, and shear-layer instability. The latter mechanism, also called Kelvin-Helmholtz instability, is a crucial phenomenon which has been investigated previously only with over-simplified theoretical models and room-temperature physical models using surrogate fluids, both of which behave very differently from steel casters. This paper critically reviews previous literature on entrainment mechanisms. It then presents a realistic numerical model to investigate the Kelvin-Helmholtz entrainment mechanism in steel continuous casters and validates it with a simplified analytical solution of this phenomenon. Finally, the critical meniscus velocity to avoid mold flux entrainment via this mechanism is briefly discussed.

INTRODUCTION

Mold flux/slag entrainment, also called emulsification, entrapment, involvement, or engulfment is an important problem in the production of clean steel. By any name, this phenomenon of interest in this work is characterized by droplets of melted mold powder being drawn into the molten steel pool inside a continuous casting mold. Mold flux entrainment can cause both surface and internal defects if the entrained particles become trapped in the solidifying steel. All of the previous work on this subject, regardless of the analysis method or entrainment mechanism, agrees that mold flux entrainment depends mainly on the physical properties of the materials involved (especially the density, viscosity, and interfacial tension of the steel and slag); the slag layer thickness; and flow system design and operating conditions (especially nozzle geometry, casting speed, and argon gas flow rate).

Flux entrainment has received much attention over the years and several different mechanisms have been proposed, and are summarized in this work. Many studies have used room-temperature physical models, usually with water and a silicon oil to simulate the molten steel and slag of the continuous caster. Physical models are unable to match all of the relevant similarity criteria simultaneously, however, so their results are difficult to interpret quantitatively. Capturing the fluid flow pattern and meniscus level profile requires matching the Froude number, and perhaps also the Reynolds number¹. This leaves Weber similarity unsatisfied, so interfacial tension effects are not properly reproduced. The surrogate liquid properties can be changed with additives, but this usually changes more than one property; *e.g.* an additive to change interfacial tension may also change density, so it is difficult to isolate the individual effects. Interfacial tension is also difficult to measure, especially considering that it is a time-dependent phenomenon. The ever-advancing computer technology and improving computational fluid dynamics (CFD) models have also allowed numerical investigations of flux entrainment, although they still face challenges including the inherent transient nature of turbulent flow, multi-phase discretization schemes, and mesh resolution. The computational models referred to in this paper include both in-house and commercial codes, using both finite-volume and finite-element methods. Turbulence is most often treated with the k - ϵ model, though other models find occasional use.

Previous reviews of work on this topic include those of Herbertson *et al.*², Suzuki *et al.*³, and Thomas⁴, but a comprehensive picture of the mechanisms of mold flux entrainment remains elusive. Early work focused mainly on fluctuations of the meniscus level, which

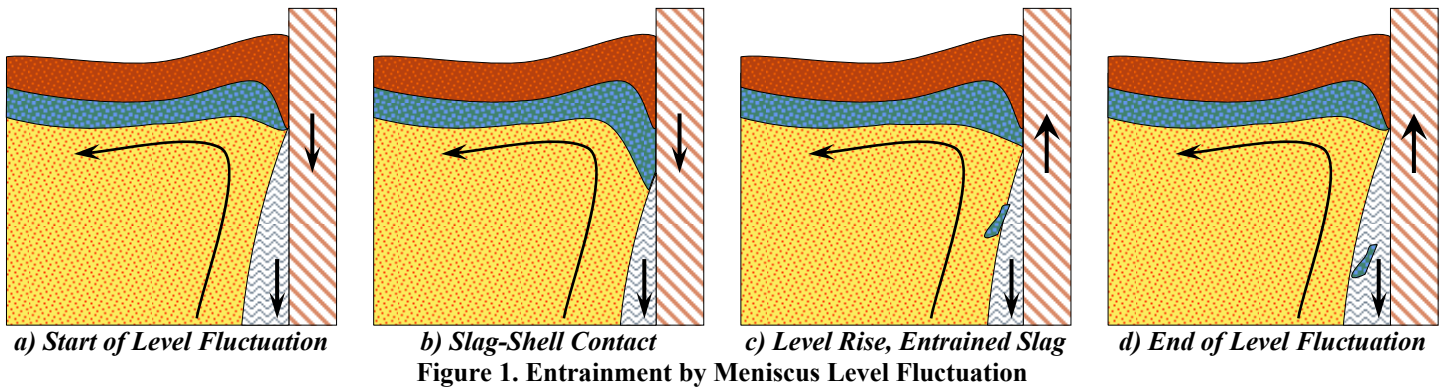
correlate strongly with defects. The entrainment mechanisms reported in later literature fall into eight more families: meniscus freezing, argon bubble interaction, slag “crawling” down the submerged entry nozzle (SEN), vortexing, meniscus standing wave instability, shear-layer (Kelvin-Helmholtz) instability, narrow face spout impingement upon the meniscus, and meniscus balding. Most mechanisms suggest a critical condition for entrainment, which can be used as a practical evaluation of physical or numerical models of fluid flow in a caster.

Entrainment is not detrimental to product quality unless the inclusions become caught in the solidifying steel. A numerical study showed that particles may or may not become entrapped in an approaching dendritic solidification front depending on the particle diameter, local crossflow velocity, and steel composition⁵. Downward flow velocities may exacerbate entrapment by suspending the rising particles in front of the solidifying interface⁶, which may explain why single-roll patterns are found to produce more slag entrapment defects⁷. Numerical models have shown that the flow pattern in the mold should deliver 70% of large (400- μm) particles to the slag layer, but less than 10% of small (10- to 40- μm) particles⁵. The capacity of the liquid slag layer to absorb the inclusions that reach it depends greatly on the composition, and associated properties⁸. Dynamic models have been constructed for solid⁹ and liquid¹⁰ particles to determine if a particle will be absorbed into the slag layer, which decreases with decreasing inclusion particle diameter, decreasing wettability between the slag and particles, increasing interfacial tension, and increasing slag viscosity. However, as discussed below, these same properties which discourage inclusion removal often help to prevent entrainment from occurring at all.

This paper first presents a critical overview of the nine families of mechanisms that cause entrainment of mold slag during continuous casting, focusing on quantitative prediction of the critical conditions for each mechanism. The review adopts the following symbols: V is velocity, g is acceleration due to gravity, μ is molecular viscosity, ρ is density, and Γ_{AB} is interfacial tension between fluids A and B . The subscript u refers to the *upper* fluid layer (melted mold powder or oil, etc.) and the subscript ℓ refers to the *lower* fluid layer (molten steel or water, etc.). The immersion depth of the SEN h_{SEN} is the vertical distance between the meniscus level and the top edges of the ports. SEN port angles decrease when pointing more steeply downwards. The paper then introduces a computational model to simulate one of these mechanisms, shear-layer instability. The numerical model is validated with an analytical solution, and preliminary implications are suggested.

Meniscus Level Fluctuations

Many early studies on slag entrainment mechanisms focused on transient fluctuations of the meniscus, because they are observable and measurable in the steel plant. However, recent numerical models^{11,12} showed how level fluctuations can entrain slag by exposing the dendritic interface of the top of the solidifying steel shell to liquid slag and mold powder during a sudden drop in the level. Figure 1 shows the sequence of events leading to entrainment by this mechanism. Although oscillation causes slight changes in liquid level during each cycle, transient changes in the flow pattern in the mold are responsible for the large level fluctuations that cause severe slag entrainment defects.



Physical model studies have shown that meniscus fluctuations increase with increasing casting speed^{13,14}, increasing SEN bore diameter¹⁵, increasing SEN port angles^{13,15}, decreasing SEN immersion depth¹³, decreasing slab width¹³, and increasing argon flow rate^{13,15,16}. Poor wettability between the argon and SEN refractory increases the effect of argon on fluctuations¹⁶, but increasing the casting speed decreases the effect of argon bubbles¹³. Meniscus fluctuations can be suppressed in physical models with the proper combination of SEN immersion depth, argon injection rate, and nozzle geometry, but these depend on casting speed and mold width¹⁷. For example, turbulence of the meniscus in physical models has been observed, by direct observation¹⁸ and measurements of turbulent kinetic energy¹⁹, to increase sharply with decreasing immersion depths; lower than a critical immersion depth, however, the meniscus is relatively quiet. The optimal flow pattern also depends on many other casting parameters, such as mold thickness and shape: thin-slab casters experience different level fluctuation behavior than thick-slab casters. Electromagnetic forces offer another variable to control the flow pattern. Plant experiments using electromagnetic braking have reported decreases in level fluctuations and associated defects (*cf.* the review in the paper by Cukierski and Thomas²⁰). Other plant experiments have reported the use of traveling electromagnetic field stirring to control fluctuations and significantly reduce the number of defects¹⁴.

Direct observation of the meniscus in an actual caster²¹ revealed that most meniscus fluctuations have the same frequency as the mold oscillations, though the fluctuation amplitude is about 70% of the oscillation amplitude. This percentage was observed to increase with casting speed. Half-scale water modeling studies²², without a slag layer, revealed that meniscus fluctuations were found to be relatively insensitive to SEN immersion depth (100-140 mm) and casting speed (0.8-2.3 m/min). The meniscus was observed to fluctuate with frequencies of about 0.2 Hz, corresponding to fluctuations at the nozzle ports²², and with frequencies of about 2 Hz^{22,23}, corresponding perhaps to the mold oscillation frequency. The slag layer damps out higher frequency fluctuations sooner than without a slag layer²⁴. Meniscus fluctuations can also be caused by changes in upstream flow control devices, such as a stopper rod or slide gate²⁴. Honeyands and Herbertson²⁵ observed periodic flow oscillation between the left and right sides of the mold in water model experiments at high casting speed. The oscillations are caused by a perpetual competition between pressure gradient in the mold and jet momentum, and cause peak surface velocities near 1m/s and corresponding oscillations in the surface wave profile. The oscillation frequencies f scale by the Strouhal number $f \cdot h_{SEN} / V_C$, where V_C is the casting speed.

Teshima *et al.*¹³ characterized the effect of SEN and mold geometry on the strength of flow up the narrow face with the “ F Value”:

$$F = \rho_t Q V_{coll} (1 - \sin \theta_{coll}) / 4 h_{coll} \quad (1)$$

where Q is the total flow rate through the nozzle. The jet impinges onto the narrow face with collision speed V_{coll} and angle below horizontal θ_{coll} , and h_{coll} is the depth below the meniscus of the collision (impingement) point, as illustrated in Figure 2. The level fluctuation severity increases linearly with the “ F Value”¹³, especially near the narrow face. Plant measurements¹⁴ showed that the largest fluctuations A (in mm) can be estimated by multiplying F (N/m) by 3. The collision speed increases with increasing casting speed and decreasing slab width^{15,18}, and can be estimated using physical or numerical models.

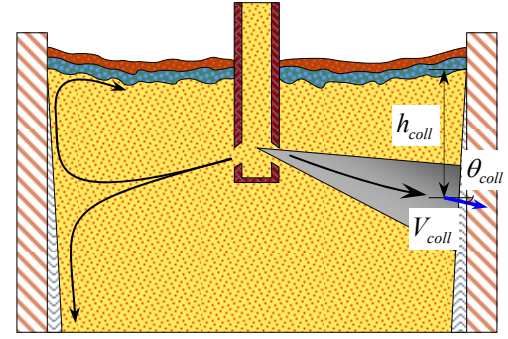


Figure 2. “ F Value” Model Description

Numerous plant experiments showed that keeping the “ F Value” between 3 and 5 N/m¹³ (grade not given), or between 2 and 3 N/m²⁶ for a low-carbon aluminum-killed steel results in slabs with good surface quality¹⁴. The largest level fluctuations (in mm) and F value are both related to the velocity of the steel stream just below the surface slag layer, $V_{surface}$ (in m/s)¹⁴:

$$A = 3F = 35V_{surface} \quad (2)$$

Combining this correlation with the critical F range leads to a prediction of the critical near-surface velocity range to avoid defects of about 0.2 to 0.4 m/s¹⁴. However, critical surface velocities for slag entrainment arise from other mechanisms discussed in the next sections. For example, another prediction²⁷ of critical maximum surface velocity to avoid slag entrainment V_{crit} is:

$$V_{crit} = \sqrt{(2/\rho_u)} \sqrt{12\Gamma_{ul} g (\rho_t - 3\rho_u) - 2gA} \quad (3)$$

which is limited to slags with density less than 1/3 of steel. The lower limit arises in reality to prevent defects arising from meniscus freezing, hook formation, and the entrapment of rising slag particles. These cross-correlations make it difficult to determine the real mechanisms responsible for slag entrainment defects. The next sections discuss each of these other mechanisms in turn.

Meniscus Freezing and Hook Formation

Another mechanism for the entrainment of slag and inclusion particles to form surface defects is illustrated in Figure 3, which shows a slag particle entrapped by a hook. The root cause of hook formation^{28,29} is freezing of the meniscus, due to insufficient heat delivered to the meniscus region, particularly near the narrow face, where temperatures tend to be lowest. The frozen meniscus may extend into the melt and can capture rising bubbles, slag droplets, or solid inclusions. In addition, overflowing of the frozen meniscus can entrap any slag coating its surface. Hooks can be prevented by increasing superheat, increasing SEN port angles, or increasing flow velocity, all of which increase the heat supply to this region. This mechanism explains the lower limit on surface velocity and the accompanying level fluctuations observed in plant correlations discussed in the previous section.

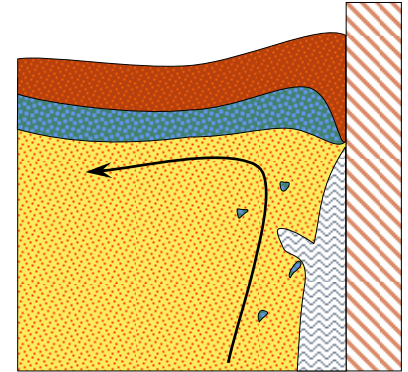


Figure 3. Hook Trapping Rising Particle

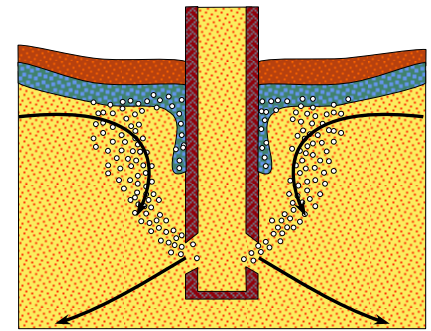
Flow conditions such as caused by a shallow SEN may produce excessive meniscus surface velocities which increase surface turbulence, leading to instability, entrapment, and uneven powder distribution, as discussed in the previous section. However, too deep

an SEN can result in meniscus freezing, hook formation, and shell thinning below mold exit¹⁸. Kubota¹⁴ demonstrated that EMBR may be used to increase flow velocities at lower casting speeds/higher widths to avoid hook formation, and gave the condition that surface velocities should be kept above a lower limit of 0.15-0.25 m/s to minimize surface defects for the mold considered in the study.

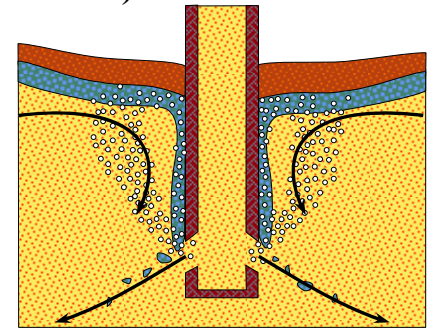
Argon Bubble Interactions

Gas bubble interaction leads to another family of slag entrainment mechanisms. Argon gas is usually fed into the SEN to help prevent nozzle clogging, which leads to problems from both nonmetallic inclusions and asymmetric fluid flow. Argon bubbles also add a buoyancy force to the steel flow that lifts the jet up to the steel/slag interface, and changes the flow pattern. Thus, argon injection may lessen some problems, such as hook formation, but is detrimental to other entrapment mechanisms, such as surface level fluctuations. In addition, inclusions and slag can coat the surface of argon bubbles, leading to large defects if entrapped into the final product. Clearly, the interactions of argon bubbles with the molten steel and slag layer are complex phenomena.

Emling *et al.*³⁰ found product defects caused by argon gas bubbles coated with mold slag. They noted in a water model study that argon bubbles flowing out of the SEN can form a foam with the slag layer, which can adhere to and crawl down the outside of the nozzle and become caught in the stream exiting the nozzle, entraining large amounts of slag, as illustrated in Figure 4. The formation of slag foam leads to slag-entrainment defects even though mold surface velocity and level fluctuations were small³⁰. The occurrence of the foam was found to increase with decreasing bubble diameters, increasing slab width, increasing argon injection rates, increasing slag viscosity, decreasing slag density, and decreasing interfacial tension between the slag and steel. The critical argon flow rate to avoid slag foaming depends on the liquid throughput; higher throughputs causes smaller bubbles which have little inertial forces and follow the steel flow pattern. Plant trials showed a reduction in pencil pipe defects when the gas flow rate was reduced³⁰. Later physical model experiments showed that this critical gas injection rate decreases with increasing casting speed, decreasing slag layer viscosity, decreasing nozzle port angles, and decreasing wettability between the SEN material and molten slag¹⁶. However, other plant trials³¹ showed that the number of pencil blister defects was strongly correlated with overall throughput and relatively insensitive to other variables, including argon flow rate, SEN port angles, port diameters, and submergence depth.



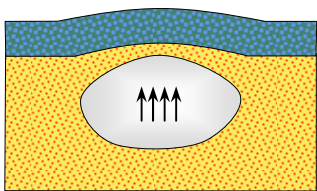
a) Foam Formation



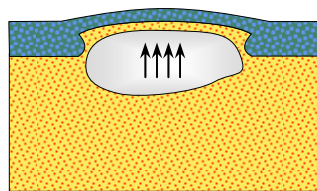
b) Entrainment Due to Slag Foam

Figure 4. Slag Foaming

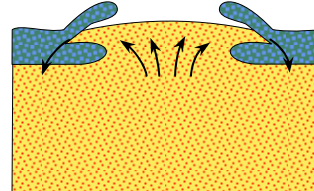
As a bubble rises into and through the molten slag layer, a thin film of molten steel is caught between the bubble and slag. If and when the bubble breaks through to atmosphere, the film of steel will be trapped in the slag layer, until gravity pulls it back into the melt, possibly bringing some slag with it^{32,33}, as shown in Figure 5. However, the flow inside the liquid slag layer^{34,35} and constraint provided by the sintered slag layer³² forces the bubbles to move laterally towards the SEN or narrow face, somewhat mitigating the entrainment by this mechanism. Physical model investigations revealed that the maximum depth the slag is carried downwards into the molten steel after bubble penetration into the slag layer was consistently about three times the bubble diameter³². Smaller bubbles were observed not to rupture the slag layer at all³³. The physical properties of the fluids had almost no effect on this phenomenon, except that increasing interfacial tension likely decreases the slag entrainment³². Other water-modeling work^{16,33} noted that the oil layer was drawn downward via capillary forces along the gas-filled spaces of the rough surface of the SEN, which was coated with a wax to decrease wettability. This capillary action might also be an entrainment mechanism in actual continuous casting molds.



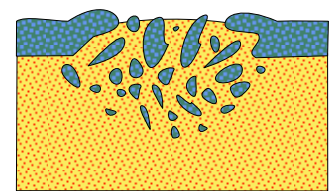
a) Approaching Bubble



b) Penetrating Bubble



c) Slag Layer Rupture



d) Entrainment after Rupture

Figure 5. Slag Entrainment by Bubble Penetration of Slag Layer

Slag Crawling

A solid object submerged into a flowing liquid will result in a pressure buildup on the windward (right) side and a corresponding pressure drop in the leeward (left) side, as illustrated in Figure 6. When a free surface is present, these pressure changes will cause changes in elevation of the surface. Asymmetric flow in a continuous casting mold can cause this situation to occur. This low-pressure zone might draw some liquid mold slag down along the leeward outside of the SEN, shown in Figures 6a and 6c. If severe enough, the slag might become entrained into the steel jet and be carried away to form defects, as shown in Figure 6b.

Asymmetric flow in the mold has several causes, including nozzle clogging^{19,36}; argon bubbles coalescing in the SEN to send more large bubbles out one port than the other; asymmetric flow across the bottom of the tundish^{37,38}; stopper rod misalignment⁶; use of a slide-gate mechanism to control flow^{39,40}; and transient turbulent flow variations even while the time-averaged flow pattern is symmetrical⁴¹, and other random asymmetries. The tendency for asymmetric flow was found to increase with increasing slab width, owing to the higher throughput and a larger possible difference between impingement points on opposing narrow faces¹⁸.

Physical model experiments of flow past a circular cylinder in a rotating trough⁴² were performed to investigate the effect of fluid properties on this mechanism. For casters with the ratio of SEN outer diameter to slab thickness, or “blockage factor” between 0.4 to 0.6, the penetration depth h_p that the upper fluid crawls down the cylinder is given by:

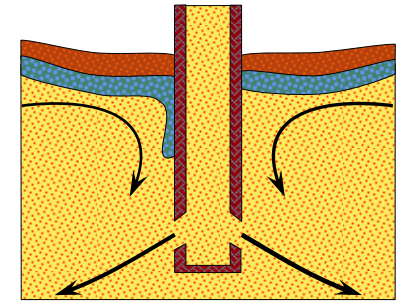
$$h_p = 1.9 \left[C_{p,\max} \rho_u V_u^2 + C_{p,\min} \rho_\ell V_\ell^2 \right] / [g(\rho_\ell - \rho_u)] \quad (4)$$

where $C_{p,\max} = 1.0$ and $C_{p,\min} = 2.5$ are the maximum and minimum pressure coefficients for a circular nozzle. The maximum occurs at the forward stagnation point (windward side) and the minimum is on the sides of the SEN, *i.e.* the closest points to the wide faces. For elliptical nozzles, a numerical parametric study⁴³ found these pressure coefficients to decrease with increasing aspect ratio a according to:

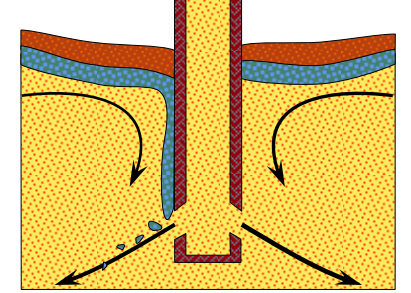
$$C_{p,\max} = 1.376 - 0.0652 \cdot a \quad (5)$$

$$C_{p,\min} = 1.978 - 1.065 \cdot \ln(a) \quad (6)$$

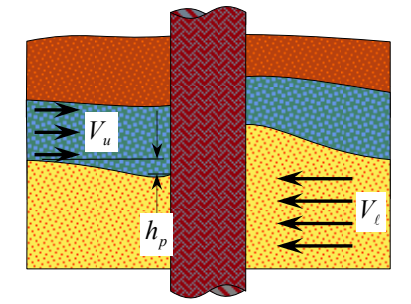
where the aspect ratio is the ratio of the major diameter (parallel to the flow direction) to the minor diameter. Thus, increasing the SEN aspect ratio should lower the penetration depth by reducing the pressure drop across the SEN. This technique might also help other flow-related defects by reducing the blockage factor, as is commonly done in thin-slab casters. To avoid entrainment by this mechanism, the SEN immersion depth should be greater than the slag penetration depth. Note that these experiments were carried out for materials with good wettability with the SEN; other models have shown that poor wettability between the oil layer and SEN material increases the penetration depth by a factor of about 1.6¹⁶.



a) Slag Crawling Initiation



b) Entrainment by Slag Crawling



c) Slag Crawling Model Features
Figure 6. Slag Crawling

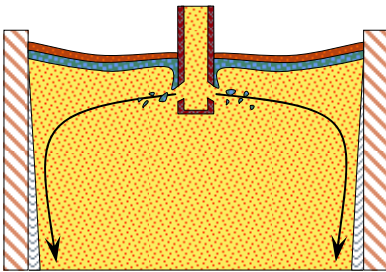


Figure 7. Shallow SEN

pressure zone in the wake of flow past the SEN, another way that asymmetric flow can induce mold slag entrainment is by vortex formation, discussed in the next section.

von Kármán Vortex Formation

Flow past bluff bodies can result in the periodic shedding of vortices in the wake of the object. Asymmetric flow between sides of the mold is the source of flow through the narrow gap between the SEN and mold walls that causes vortices that entrain slag, as shown in Figure 8. The slightest asymmetry can result in the formation of vortices, but this does not guarantee the entrainment of slag.

These vortices can entrain slag that becomes entrapped between the dendrites on the wide face near the SEN, leading to a sharp increase in the number of sliver defects in the center of the slabs¹⁸. Alternatively, vortices may pull a funnel of slag deep enough into the mold that the jet coming out of the SEN entrains the tip of the vortex, transporting slag-related inclusions elsewhere in the slab^{44,45,46}. The vortices are always observed form on the weaker (leeward) side of the flow, *i.e.*, in the wake of the SEN^{44,45,46,47,48,49,50}. Vortex depth increases with increasing meniscus surface velocity^{44,48} and vortex diameter increases with increasing SEN misalignment

in either the width⁴⁴ or thickness directions⁴⁵. Vortex formation frequency increases with increasing slab width^{18,49}, shallower SEN immersion depths^{18,46,49} with no vortices at 100 mm depths and greater⁴⁶, increasing SEN port angle^{45,46}, increasing casting speed/SEN flow rates^{18,45,46,48}, and increasing SEN misalignment^{44,45}. Vortex formation is also a function of SEN geometry^{18,49}; vortex formation was reduced by keeping the ratio of the inner diameter of the SEN to the hydraulic diameter of the SEN ports greater than 1.1¹⁸. The lifetime/duration of a vortex varies, but will eventually be damped out by viscous dissipation or changing flow characteristics^{46,48}.

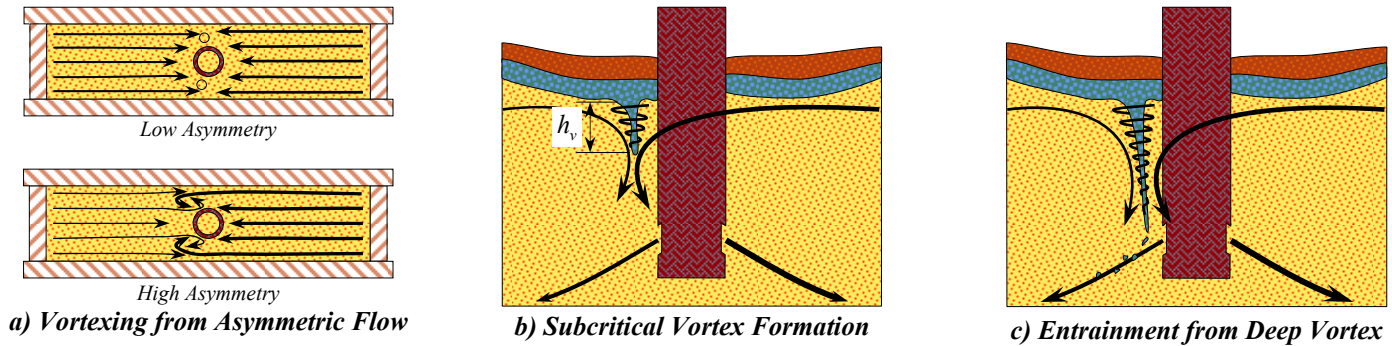


Figure 8. Slag Entrainment by von Kármán Vortex Formation

He⁴⁷ proposed that vortices are not formed by asymmetric flow alone but also require the downward momentum of flow in the upper recirculation zone at the point where the two opposing flows “butt heads,” to pull the vortex funnel downward. Asymmetric flow is reported to increase the frequency, depth, and size of the vortices. Small vortices are also observed during symmetrical casting, unless vertical walls are inserted between the SEN and the wide face walls to prevent flow through the gap. In order for a vortex to form, there needs to be sufficient rotational flow caused by flow through this gap.

Vortex formation needs both rotational flow in the plane of the meniscus, and a downward-pulling sink. The sink momentum is found where the opposing roll flows meet near the center of the mold^{47,48}. Vortices were observed on the slow side of the mold just after a peak in velocity on the opposite side⁴⁸. A sudden jump in downward velocity pulls the vortices deeper into the mold, enabling the jet to entrain slag from the tip of the funnel⁴⁶. Increasing the casting speed results in larger downward velocities and a stronger tendency for vortices to form⁴⁴. A critical jump in downward velocity of 86 mm/s was observed to be needed before vortex formation occurs. Above this limit, the occurrence frequency of vortex formation increases with further increases in the velocity jump⁴⁶. The water model studies found that vortices require a minimum velocity to form, reported as 35 L/min nozzle flow rate⁴⁶. A maximum velocity for vortex formation was also observed, because excessive velocities cause the meniscus to become too oscillatory and turbulent to allow the formation of vortices^{46,48}. However, meeting a critical meniscus velocity or flow rate criterion does not guarantee vortex formation⁴⁹, and furthermore, the presence of a vortex does not necessarily mean that slag will be entrained into the melt⁴⁶.

The direction of rotation of the vortices depends on the side of the SEN by which the vortex forms, but appears to have no bearing on entrainment⁴⁹. Vortices were observed to form both one at a time and in pairs^{46,49}. With a double-roll flow pattern, vortices formed within about 3 cm of the SEN outer wall and traveled outward to the narrow faces⁴⁶. Single-roll flow patterns, caused by shallow SEN immersion depths and wider slabs, also suffer from vortices, which form near the narrow faces instead of by the SEN⁴⁷.

Computational models confirm that vortex formation cannot occur with perfectly symmetric geometry and flow conditions^{44,51}, regardless of the mesh size and turbulence model⁵¹. In general, the more misaligned the SEN, the more asymmetric the flow pattern in the mold and the larger the vortex diameter^{44,45}. However, the amount of misalignment does not change the downward velocity that helps vortex formation⁴⁴.

Initial attempts to suppress vortex formation with flat fins protruding out of the SEN towards the narrow faces met with little success; vortex size and formation frequency remained unchanged, though the formation location was moved to the tips of the fins rather than by the SEN¹⁸. Increasing argon flow rates to above 10% gas fraction induces buoyancy that can decrease downward velocity near the SEN and prevent vortex formation, but this reinforces asymmetric flow⁴⁴, and can also trigger some of the argon-related slag entrainment mechanisms discussed above. Vortex formation was shown to be effectively suppressed with sufficiently strong EMBR to control the asymmetry of the flow^{44,50}, although this depends on SEN geometry⁵⁰. Using both argon gas and EMBR together can be effective in suppressing vortex formation for a given set of mold and SEN conditions⁴⁴.

A few quantitative predictions of vortex formation have been proposed. Vortex formation increases with increasing “F Value” given by Equation (1)¹³. Early water modeling⁵² proposed a critical SEN port velocity to prevent vortex-based slag entrainment:

$$V_{port,crit} = \sqrt{g w_{slab} \left[\frac{(\rho_l - \rho_u)}{\rho_l} \right] \left[c_1 + c_2 \left(\frac{\mu_u}{\mu_l} \right) \right]} \quad (7)$$

where the constants $c_1 = 0.1$ and $c_2 = 0.009167$ for 0-mm deep SEN wells and $c_1 = 0.35$ and $c_2 = 0.01833$ for 10-mm and deeper SEN wells. Recent water modeling⁴⁶ has proposed a critical surface velocity for vortex formation of 0.3 m/s, as well as a model to predict the depth of vortices h_v :

$$h_v = \left(v_{mc}^2 / g \right) \left[\rho_\ell / (\rho_\ell - \rho_u) \right] + C \left\{ \left(\Delta v_s^2 / g \right) \left[\rho_u / (\rho_\ell - \rho_u) \right] \right\}^{0.55} \quad (8)$$

where v_{mc} is the horizontal steel velocity (m/s) in the center of the mold, 10 mm below the water-oil interface and halfway between the SEN and wide face, Δv_s is the sudden change in vertical velocity, measured 50 mm below the steel-slag interface, 10 mm away from the SEN and halfway between the wide faces, and $C = 0.0562 \text{ m}^{0.45}$ is a constant with all other quantities in m-kg-s units. This model can be used to predict the required SEN immersion depth to avoid the jets cutting of the tips of the vortices.

The amount of slag entrained by the vortices was experimentally measured⁵³ for molten steel and several slags. Slags with higher viscosity and higher interfacial tension resulted in smaller amounts of entrained slag:

$$m = C / \left(\mu_u^{0.255} \Gamma_{u\ell}^{2.18} \right) \quad (9)$$

where m is the mass of the entrained particle, in grams, and $C = 3.057 \cdot 10^{-3} \text{ kg}^{3.435} \text{ m}^{-0.255} \text{ s}^{-4.615}$ is a constant, μ_u is the slag viscosity in Pa·s, and $\Gamma_{u\ell}$ is the interfacial tension in N/m. This relation can be used to predict droplet size and corresponding terminal velocity, or with a particle entrapment/engulfment model to predict inclusion behavior.

Meniscus Standing Wave Instability

Flow beneath a free liquid surface will create surface waves which can become unstable and turn over to entrain the interface, if the local slope becomes sufficiently steep (exceeding vertical)⁵⁴. In the mold, this flow leads to a stationary wave in the surface shape, excluding the local level fluctuations discussed previously. For so-called “double-roll” flow patterns, the surface shape is raised at the narrow faces. The standing wave may also become unstable if the vertical acceleration of the fluid is anywhere greater than the gravitational acceleration, although this appears not to be a problem in practice²³. Rottman⁵⁴ numerically investigated the stability of two-dimensional standing waves at the interface between two semi-infinite inviscid and incompressible fluids of different but uniform densities in irrotational flow. A stability criterion was fit from these results as a height-to-wavelength ratio⁵⁵:

$$\left(h_{\text{wave}} / \lambda \right)_{\text{critical}} = 0.21 + 0.14 \left(\rho_u / \rho_\ell \right)^2 \quad (10)$$

where h_{wave} is the wave height defined as the vertical distance between the lowest point (trough) and highest point (crest) of the surface level and λ is the wavelength, defined as the distance between the outer SEN wall and the narrow faces^{23,55,56}. Rottman noted that as the density ratio ρ_u / ρ_ℓ decreases, the higher harmonics of the wave are damped out, and the point of vertical slope shifts from the midpoint of the wave towards the crest⁵⁴. Rottman also noted that earlier experiments indicated this model was an overprediction and that a vortex forms at the node at lower height-to-wavelength ratios, indicating that the stability of the wave is governed by shearing at the interface, rather than by the wave turning over⁵⁴.

Although derived for conditions different from a continuous caster, the condition of Rottman has been used in various models to classify the critical wave height, including studies based on a single-phase water model⁴⁹, and its corresponding computational model²³. Other researchers²² proposed another relation based on level fluctuations in a water model:

$$\text{Gupta and Lahiri}^{49}: h_{\text{wave}} = 0.577 \left(V_{\text{port}}^2 / g \right) \left(D_{\text{port}} / L_c \right) \quad (11)$$

$$\text{Moghaddam et al.}^{22}: h_{\text{wave}} = 0.12 \left(V_{\text{port}}^2 / g \right) \left(D_{\text{port}} / L_c \right) \quad (12)$$

$$\text{Panaras et al.}^{23}: h_{\text{wave}} = 0.41 \left(V_{\text{port}}^2 / g \right) \quad (13)$$

where D_{port} is the diameter of the SEN ports, V_{port} is the velocity of the water/molten steel at the SEN ports, and L_c is a characteristic length taken as the height of the upper recirculation zone, calculated as $L_c = h_{\text{SEN}} + \frac{1}{2} w_{\text{slab}} \tan \left(\phi_{\text{discharge}} - \frac{1}{2} \phi_{\text{jet}} \right)$ for immersion depth h_{SEN} , slab width w_{slab} , jet discharge angle $\phi_{\text{discharge}}$, and jet spread angle ϕ_{spread} , as shown in Figure 9. The jet spread and discharge angles vary with SEN bore diameter, port diameter, well depth, and nominal port angles^{40,57,58}. The jet impingement point was reported to shift downward about 25-50 mm for every 0.2 m/min increase in casting speed¹⁸.

The effect of the slag layer is to increase the surface wave height as follows, based on oil-and-water physical models⁵⁹ and two-dimensional, two-phase numerical models of those physical models⁵⁵:

$$\text{Gupta and Lahiri}^{59}: h_{\text{wave}} = 0.577 \left(V_{\text{port}}^2 / g \right) \left(D_{\text{port}} / L_c \right) \left[\rho_{\ell} / (\rho_{\ell} - \rho_u) \right] \quad (14)$$

$$\text{Theodorakakos and Bergeles}^{55}: h_{\text{wave}} = 0.31 \left(V_{\text{port}}^2 / g \right) \left(D_{\text{port}} / L_c \right) \left[(\rho_{\ell} + \rho_u) / (\rho_{\ell} - \rho_u) \right] \quad (15)$$

The behavior of the meniscus is well known to be a function of the flow pattern, which depends on other conditions and SEN design, so the coefficients in Equations (11) to (15) have limited applicability outside of the conditions for which they were derived. Nevertheless, all models contain V_{port}^2 / g , indicating that meniscus height scales with the dynamic head of the flow out of the SEN ports. These models can be used with Equation (10) to predict a critical maximum port velocity to avoid an unstable surface wave.

The wave height h_{wave} increases with increasing casting speed, which generally increases all velocities in the melt pool. In contrast with the quadratic relationship given in Equations (11) to (15), some report a linear relationship²⁵, while others report something in between^{56,60}. The wave height also increases with higher SEN port velocities, larger diameter SEN ports (up to a limit), shallower SEN immersion depths, SEN port angles aimed more upward, narrower mold widths^{23,49,59,55,56,60,25}, and lower mold thickness¹. Three-dimensional numerical modeling work showed that wavelength λ_{wave} also depends on SEN immersion depth⁵⁶.

A few modelers built on the initial work of Bergeles and colleagues^{23,55,56}, who assumed isothermal flow and were unable to simulate the wave instability event. The simplified surface tension model was improved with a two-dimensional, two-phase (air and water), isothermal numerical model⁶¹ of the early physical experiments⁴⁹, and successfully simulated the wave turnover event and the resulting entrapment of air bubbles at the trough of the wave. This numerical model showed a recirculating packet of fluid at the trough and disappeared after entrainment. This suggests that shear stresses form a horizontal vortex that causes the instability of the interface, which is a different mechanism, discussed in the next section. The highest surface velocities coincide with the trough of the standing wave^{52,56,61}, which again indicate that shear instability is the real cause of entrainment. A three-dimensional, single-phase, model⁶⁰ included the effect of temperature gradients and buoyancy forces, and calculated a large increase in wave height. Other models of thin slab casting found greatly increased surface velocities caused by the deflection of the flow pattern by the solidifying steel shell^{1,62}. None of these models investigates a real steel-slag system or asymmetry and the different phenomena have not yet been tied together using a single model. However, it appears likely that the standing wave height instability (turnover) mechanism is not a problem in practice, because shear instability occurs more easily.

Shear Layer Instability

The interface between two density-stratified fluids with relative motion will become unstable with a large-enough difference in velocity. A theoretical condition for this instability was derived by Helmholtz⁶³ and Kelvin⁶⁴ for two inviscid, irrotational fluids of different density separated by a flat interface and moving at different horizontal velocities. Most researchers have identified shear instability of the interface to be a cause for mold slag entrapment, shown in Figure 10, which is exacerbated by turbulent fluctuations¹⁹, though little has been done to explore this mechanism.

This fundamental hydrodynamic phenomenon of Kelvin-Helmholtz instability has received considerable treatment over the last 150 years and is found throughout nature, including ocean waves and clouds. The interface between the two fluids becomes unstable and emulsifies when the velocity difference between the two layers is greater than:

$$\Delta V_{\text{crit}} = \sqrt{\left[\frac{1}{\rho_{\ell}} + \frac{1}{\rho_u} \right] \left[\frac{g}{k} (\rho_{\ell} - \rho_u) + k \Gamma_{ul} \right]} \quad (16)$$

where $k = 2\pi/\lambda$ is the (angular) wavenumber of a small perturbation on the interface with wavelength, λ . Above this velocity difference, Equation (16) predicts that the small perturbations grow without bound and form the characteristic billows simulated later in this paper. The minimum critical velocity occurs at the capillary wavelength, where instabilities usually first occur in nature:

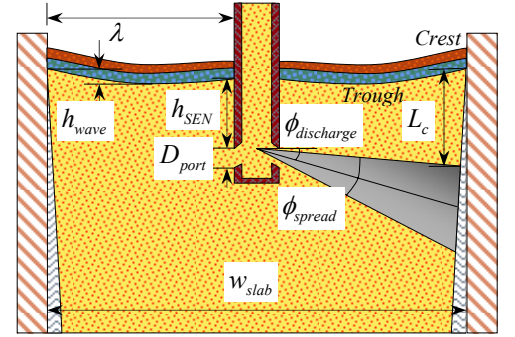


Figure 9. Standing Wave Instability

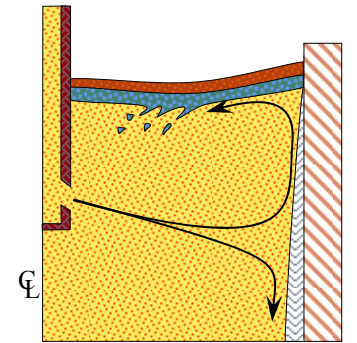


Figure 10. Shear-Layer Instability

$$\Delta V_{crit,min} = \sqrt[4]{4g(\rho_\ell - \rho_u)\Gamma_{u\ell} \left[\frac{1}{\rho_\ell} + \frac{1}{\rho_u} \right]^2}, \quad \lambda_{min} = 2\pi \sqrt{\frac{\Gamma_{u\ell}}{g(\rho_\ell - \rho_u)}} \quad (17a,b)$$

Chandrasekhar⁶⁵ extended the Kelvin-Helmholtz theory to include the effects of a uniform magnetic field. The result is not affected by a magnetic field directed transverse to the flow direction, *i.e.* DC electromagnetic flow control. A magnetic field applied parallel to the flow direction stabilizes the interface similar to surface tension. Recent numerical studies of a continuous caster⁶⁶ generalized this work to include surface tension and induced current effects by allowing the steel to be a finite conductor. The parallel magnetic field adds to surface tension and so dampens out more instabilities, but the critical velocity remains the same and the instabilities grow faster when the limit is exceeded. Funada and Joseph⁶⁷ extended the Kelvin-Helmholtz theory to include viscosity:

$$\Delta V_{crit,min} = \sqrt[4]{4g(\rho_\ell - \rho_u)\Gamma_{u\ell} \frac{(\mu_\ell + \mu_u)^4}{(\rho_u\mu_\ell^2 + \rho_\ell\mu_u^2)^2}} \quad (18)$$

This prediction has the same minimum perturbation wavelength, *i.e.* the capillary wavelength. Milne-Thomson⁶⁸ extended Kelvin-Helmholtz to include finite-depth fluid, but neglected both viscosity and surface tension, giving:

$$\Delta V_{crit} = \sqrt{g(\rho_\ell - \rho_u) \left(\frac{H_u}{\rho_u} + \frac{H_\ell}{\rho_\ell} \right)} \quad (19)$$

where H_u and H_ℓ are the thickness of the upper and lower layers. Iguchi *et al.*⁶⁹ performed physical model experiments with a covered rotating trough and confirmed Equation (19) for low-viscosity oils and low-frequency perturbations where surface tension is not important. This shear instability mechanism is most likely midway between the narrow face and the SEN where the horizontal surface velocity is a maximum. Although it needs further work to predict, it is one of the most important causes of slag entrainment.

Upward Flow Impinging on Meniscus

The upward spout along the narrow faces resulting from a double-roll flow pattern may cause slag entrainment in several ways, including both dragging⁷⁰ and cutting³⁰ modes, as illustrated in Figures 11 and 12. This is an example of shear-layer instability where the additional geometric aspects of the flow render the Kelvin-Helmholtz theory inapplicable.

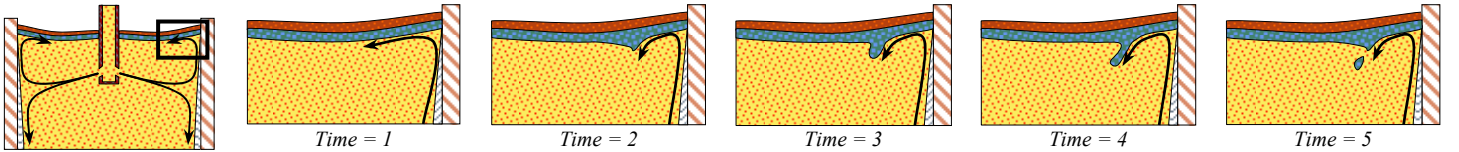


Figure 11. Slag Entrainment by Narrow Face Spout Impinging Flow, Mode I (Dragging)

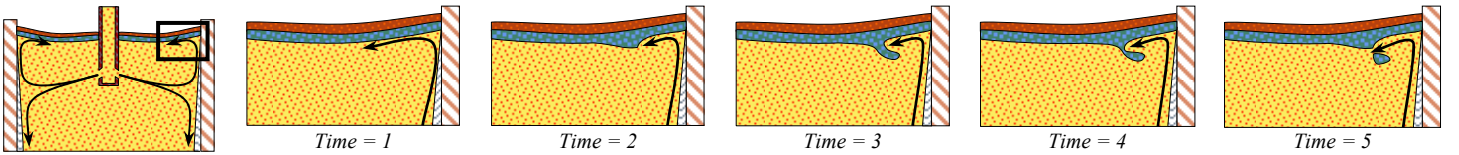


Figure 12. Slag Entrainment by Narrow Face Spout Impinging Flow, Mode II (Cutting)

Using laser-image velocimetry, Emling *et al.*³⁰ measured a critical near-surface velocity of 11.6 cm/s for this mechanism. Harman and Cramb⁷⁰ later developed the following relation, based on fitting room-temperature measurements of oil-and-water model experiments, using a submerged hose aimed at a wall to generate the upward spout of the rolling flow pattern found in continuous casting molds:

$$V_{crit} = 3.065 \left(\Gamma_{u\ell}^{0.292} g^{0.115} / \delta^{0.365} \right) \left((\rho_\ell - \rho_u)^{0.215} / \rho_u^{0.694} \right) \left(\mu_u^{0.231} / \mu_\ell^{0.043} \right) \quad (20)$$

Entrainment occurs more easily with lower water (steel) density, lower interfacial tension, lower oil (slag) viscosity, and increasing slag layer thickness δ . The measured entrainment velocities were extremely sensitive to the interfacial tension, but it must be noted that the water density and surface tension were changed together. The critical entrainment velocities predicted by this relation are likely not quantitative in a steel-slag system, but its predictions are not unreasonable. Several droplets were entrained by the shearing flow, and the diameter of the droplet first produced was always the largest⁷⁰. The diameter of the first entrained droplet is given by:

$$D = 0.534 \left[\Gamma_{u\ell}^{0.693} / \left(g^{0.564} (\rho_\ell - \rho_u)^{0.130} \rho_\ell^{0.306} \right) \right] \left(\mu_u^{0.114} / \mu_\ell^{0.372} \right) \quad (21)$$

which might be useful for modeling particle transport, entrapment, and removal. Savolainen *et al.*⁷¹ repeated this work for a wider property range and more controlled flow patterns and report similar trends, except for the effect of slag layer thickness. Differences are expected due to variations in the angle of attack of the water jet. The most important parameters for emulsification, in order, were interfacial tension, density difference, viscosity, and slag layer thickness. Earlier water modeling studies⁷² suggest that entrainment occurs at a critical density-modified Weber number of 12.3, giving the critical surface velocity as:

$$V_{crit} = \sqrt{12.3 \frac{\sqrt{\Gamma_{ul} g (\rho_l - \rho_u)}}{\rho_l}} \quad (22)$$

However, others have suggested that such simple Weber-number relationships are unable to make accurate predictions in complicated real systems, such as a continuous casting mold⁷¹.

A balance between inertia, surface tension, and buoyancy provides a prediction⁷³ of the critical velocity of the slag-metal interface and corresponding diameter of the entrained droplet:

$$V_{crit} = \sqrt{\frac{8}{\rho_u} \sqrt{\frac{2}{3} \Gamma_{ul} g (\rho_l - \rho_u) \cos(\alpha)}}, \quad D = \sqrt{6 \cdot \sec(\alpha) \frac{\Gamma_{ul}}{g (\rho_l - \rho_u)}} \quad (23a,b)$$

where α is the angle of the interface from the direction of gravity (vertical). An alternative criterion¹⁵, which assumes entrainment occurs when the radius of curvature of the interface becoming smaller than the droplet radius, gives the critical velocity and corresponding droplet size as:

$$V_{crit} = 2 \sqrt{\frac{2}{\rho_l} \sqrt{g (\rho_l - \rho_u) \Gamma_{ul}}}, \quad D = 2 \sqrt{\frac{\Gamma_{ul}}{g (\rho_l - \rho_u)}} \quad (24a,b)$$

where D is the entrained droplet diameter. Increasing the slag viscosity should lower the critical entrainment velocity for a given particle diameter. However, higher viscosity slags are observed to produce larger diameter droplets for a given velocity¹⁵.

A similar entrainment mechanism occurs in ladle metallurgy. Combined oil-and-water physical model experiments with corresponding multiphase numerical modeling^{74,75,76} of a flow system similar to that discussed above shows that shear-layer instability is the dominant mechanism in forming emulsions in ladles. The shear flow first forms a ‘lip’ at the interface which grows into a ‘ligament,’ which at higher velocities breaks up into droplets of various sizes. This chain of events was observed to be periodic, with a period of about 300-350 ms for the oils and velocities considered. Both the physical and numerical models gave that the velocities in the oil layer are about an order of magnitude lower than the velocities in the water, meaning shearing momentum transfer is small. The critical surface velocity was predicted to be about 0.26 m/s, but using higher (5x) viscosity oil makes the ligaments thicker and the droplet formation require a slightly higher critical velocity.

Meniscus Balding

In the course of exploring the various entrainment mechanisms, it was observed⁵² that the impinging flow upon the meniscus can push the slag layer out of the way, shown schematically in Figure 13. This phenomenon was termed “balding of the meniscus,” as it exposes molten steel to the atmosphere, if not the sintered and solid powder layers of the slag layer. This well-known phenomenon in ladle refining (there known as an “eye”) can also occur in continuous casting molds at higher nozzle flow rates, and the accompanying surface re-oxidation forms inclusions such as alumina. Also, particles of powder can become entrained at the bald meniscus, especially if the bald spot coincides with the trough of the standing wave⁵². Meniscus balding may be prevented by having a minimum slag layer thickness at least the size of the standing wave height⁵⁹, such as predicted from one of Equations (11) to (15). Meniscus balding can also be caused by excessive argon flow rates⁷⁷, as illustrated in Figure 14.

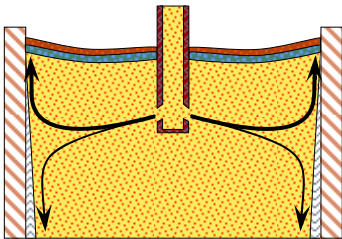


Figure 13. Meniscus Balding from Excessive NF Spout

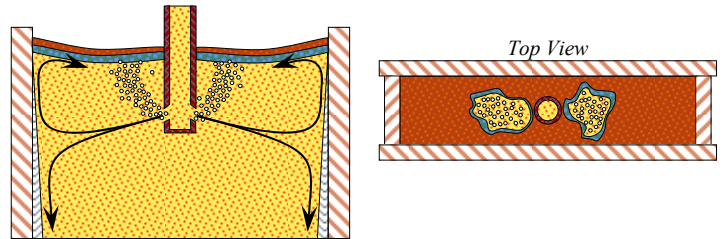


Figure 14. Meniscus Balding from Excessive Argon Flow

Discussion

Designing to avoid entrainment requires careful selection of many different parameters, to find a window of stable entrainment-free operation. Casting conditions must be found to simultaneously avoid each of the above mechanisms. The various equations presented here can be used together as design tools or to help evaluate the results of a numerical or physical model of flow in the caster. In using these equations, it should be noted that critical conditions for a given mechanism are often exceeded due to asymmetric flow conditions, even though symmetric time-averaged flow conditions would have safely avoided entrainment. Uneven clogging is often responsible for such asymmetric flow patterns, with meniscus velocities easily reaching double the steady-state unclogged values¹⁹.

There is no single optimum solution. For example, the choice of slag layer properties must balance the conflicting needs to use the slag as an inclusion catcher (requiring lower interfacial tension) with preventing shear instability (requiring high interfacial tension). Further work is needed to include chemical composition and mass transfer effects at the interface, which can significantly change the interfacial tensions. The review by Cramb *et al.*⁸ summarizes the effects of different elements on interfacial tension, as well as equilibrium and nonequilibrium effects.

Entrainment by vortex formation is likely the most common mechanism, owing to the ease at which asymmetric flow can occur. The stability of the standing wave, the impinging narrow face spout, and bone fide Kelvin-Helmholtz instability are all different embodiments of the same mechanism: parallel shear-layer instability. Preventing shear instability requires control of surface velocity. Maintaining a safe surface velocity requires selection of SEN parameters and EMBr settings to avoid excessive meniscus fluctuations and shear instability, while keeping the meniscus temperatures warm enough to prevent hook formation.

To find windows of safe operation, better models and greater understanding of entrainment mechanisms are needed. As an initial step to that end, this work turns to numerical modeling of one of the mechanisms, shear-layer instability.

COMPUTATIONAL MODEL

The stability of the steel-slag interface in shear was investigated with a computational fluid dynamics model using the commercial finite-volume code FLUENT 6.3⁷⁸. The model uses fixed (non-adaptive) quadrilateral cells. No turbulence model was used in this work, as initial efforts with the well-known $k-\varepsilon$ turbulence model damped out the transient effects of interest in this study. Without a turbulence model however, a fine mesh and time step is needed to resolve the length- and time-scales important to this problem.

Governing Equations

The equations that govern the motion of fluids⁷⁹ are the conservation of mass and the conservation of momentum. For a velocity vector field \mathbf{v} and variable density ρ , the transient conservation of mass is expressed by the continuity equation:

$$\frac{\partial \rho}{\partial t} + \nabla \cdot (\rho \mathbf{v}) = S \quad (25)$$

where S is a mass source. The momentum balance reflects the interaction between surface forces, body forces, and internal stresses. With a general body force vector \mathbf{b} and Cauchy stress tensor $\boldsymbol{\sigma} = -p\mathbf{I} + \boldsymbol{\tau}$ that is decomposed into the static pressure p and the extra stress tensor $\boldsymbol{\tau}$, where \mathbf{I} is the second-order identity tensor, the conservation of momentum demands:

$$\rho \frac{D\mathbf{v}}{Dt} = \nabla \cdot \boldsymbol{\sigma} + \rho \mathbf{b} = -\nabla p + \nabla \cdot \boldsymbol{\tau} + \rho \mathbf{b} \quad (26)$$

where D/Dt is the material derivative, which includes advection terms. All fluids in this work are assumed to exhibit Newtonian behavior, $\boldsymbol{\tau} = 2\mu\mathbf{D}$, where μ is the fluid molecular viscosity and $\mathbf{D} = \frac{1}{2}(\mathbf{L} + \mathbf{L}^T)$ is the rate-of-deformation tensor, which is the symmetric part of the velocity gradient tensor $\mathbf{L} = \nabla \mathbf{v}$. The momentum balance thus reduces to the familiar Navier-Stokes equations:

$$\rho \frac{D\mathbf{v}}{Dt} = -\nabla p + \nabla \cdot (2\mu\mathbf{D}) + \rho \mathbf{b} \quad (27)$$

Boundary conditions include fixed velocities at the inlet, prescribed constant pressure at the top surface and outlets, and zero-shear-stress. The velocities of all points on the interface between fluid A and B are equal, $\mathbf{v}_A = \mathbf{v}_B$, to satisfy continuity and kinematic compatibility. The interface also requires a dynamic condition to conserve momentum. The generalized Young-Laplace equation provides this balance between the stresses in the fluids and the forces transmitted along the surface, via interfacial tension:

$$\boldsymbol{\sigma}_A \cdot \mathbf{n} - \boldsymbol{\sigma}_B \cdot \mathbf{n} = 2\mu_A \mathbf{D}_A \cdot \mathbf{n} - 2\mu_B \mathbf{D}_B \cdot \mathbf{n} - (p_A - p_B)\mathbf{n} = 2\kappa_m \Gamma_{AB} \mathbf{n} + \nabla_{surf} (\Gamma_{AB}) \quad (28)$$

where \mathbf{n} is the unit normal vector on the interface that points from fluid A to B , κ_m is the mean curvature of the interface, Γ_{AB} is the interfacial tension between the fluids, and ∇_{surf} is the gradient operator “in the surface” such that $\nabla_{surf}(\Gamma_{AB})$ is a vector tangent to the interface and points in the direction in which Γ_{AB} increases most rapidly. This last term drives fluid flow caused by gradients of surface tension, commonly called Marangoni flows, corresponding to gradients of temperature, composition, and magnetic field.

Computational Model Setup

The multiphase behavior is modeled with the Volume-of-Fluid (VOF) Method⁸⁰, which for n ($= 2$ in this work) distinct fluids introduces $n-1$ new scalar field variables f_i to track the fraction of the volume of each cell that is occupied by each individual phase. With the additional constraint that the sum of the volume fractions in each cell is unity, these volume fraction variables are advected through the domain with the velocity field and a smoothed interface is reconstructed at the end of each time step using the modified High Resolution Interface Capturing (HRIC) Method⁸¹ within FLUENT. The VOF Method solves only one set of momentum conservation equations for one velocity field in the domain that is shared by all of the phases, thus satisfying the kinematic interfacial boundary condition by construction. The fluid properties used in the momentum balance equations are calculated in each cell with a volume-weighted average. For example, the molecular viscosity is given by:

$$\mu = \sum_{i=1}^n \mu_i f_i = \mu_1 f_1 + \mu_2 (1 - f_1) \quad (29)$$

Each individual phase i has its own continuity equation, slightly modified from Equation (2.1):

$$\frac{\partial}{\partial t}(\rho_i f_i) + \nabla \cdot (\rho_i f_i \mathbf{v}) = S_i + \sum_{j=1}^n (\dot{m}_{ij} - \dot{m}_{ji}) \quad (30)$$

where \dot{m}_{ij} is the mass flow rate from phase i to phase j , taken here as zero. The surface tension effects are treated as body forces for cells in which the interface is present with the Continuum Surface Force (CSF) Method⁸². The interface normal vector is calculated from the gradient of the volume fraction field, $\mathbf{n} = \pm \nabla f / |\nabla f|$, and the interface curvature is calculated from the divergence of the normal vector, $\kappa_m = \frac{1}{2} \nabla \cdot \mathbf{n}$. This problem is inherently transient and multiphase, so the Pressure Implicit with Splitting of Operators (PISO) Method⁸³ was used for the pressure-velocity field coupling. Within each time step, the PISO Method iterates between the pressure and velocity fields, allowing for larger under-relaxation factors (and thus much faster solution time over traditional algorithms like the well-known SIMPLE scheme) in the iterative solution of the equations and also a more accurate transient solution. With under-relaxation factors of 0.975 for all variables, about 25 iterations were needed per timestep (of $\Delta t = 0.005$ s) to converge the continuity equation residual to 10^{-12} and momentum equations residuals to 10^{-14} .

COMPUTATIONAL MODEL VALIDATION AND VERIFICATION

Validation of the model accuracy is the crucial first step prior to its application to the real process. To this end, the theoretical Kelvin-Helmholtz neutral stability curve is reproduced by running several simulations with varying velocity jumps and interface perturbation wavelengths. The simple rectangular domain used for this work is shown in Figure 15, and the boundary and initial conditions shown in Figure 16 are selected to match the conditions of Kelvin-Helmholtz instability problem. All cases have zero initial velocity in the upper fluid. Representative constant property values for oil and water are given in the inset Figure 18. The meshes used consisted of either $96 \cdot 10^3$ 2.5-mm square cells or $600 \cdot 10^3$ 1-mm square cells, and simulations ran for 10 seconds with a 0.005 s time step.

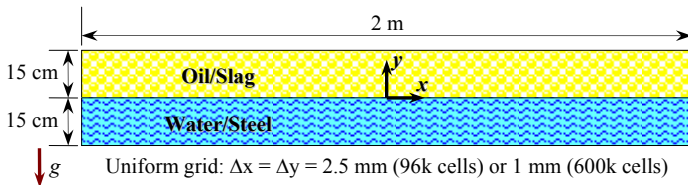


Figure 15. Model Validation Domain

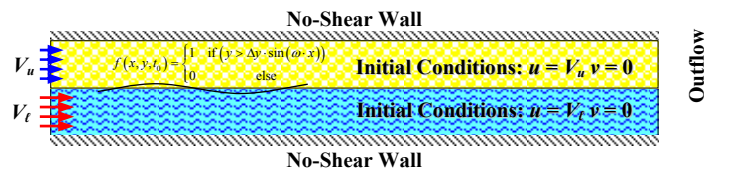


Figure 16. Model Validation Boundary and Initial Conditions

The “stable” and “unstable” results were judged from the appearance (or lack thereof) of the characteristic Kelvin-Helmholtz billows, as shown in Figures 17 and 18, where the interface is defined by the 50% volume fraction isosurface. Figure 19 shows typical simulation results for the oil-water system, which clearly match the theoretical inviscid solution. The simulation cases just below the neutral stability curve, such as $\lambda = 200$ mm, $\Delta V = 0.150$ m/s, initially formed small fingers, but did not form the full billows and hence entrainment did not occur. Increasing velocity of the lower fluid only slightly above the critical formed billows that eventually folded back into a reasonably calm interface. A large velocity jump in excess of the critical value produced more churning after the billows

formed, and clearly entrained droplets into both opposing phases. The instability predictions of Equation (16) do not necessarily imply that slag entrainment defects will occur.

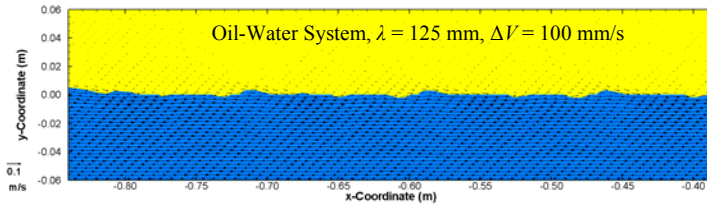


Figure 17. Perturbed but Stable Interface

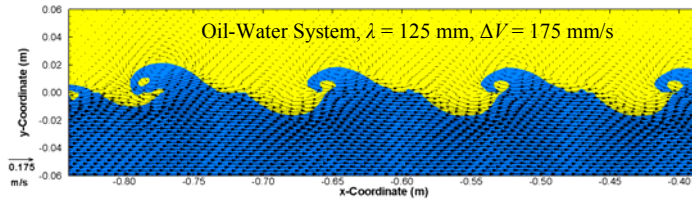


Figure 18. Kelvin-Helmholtz Unstable Interface

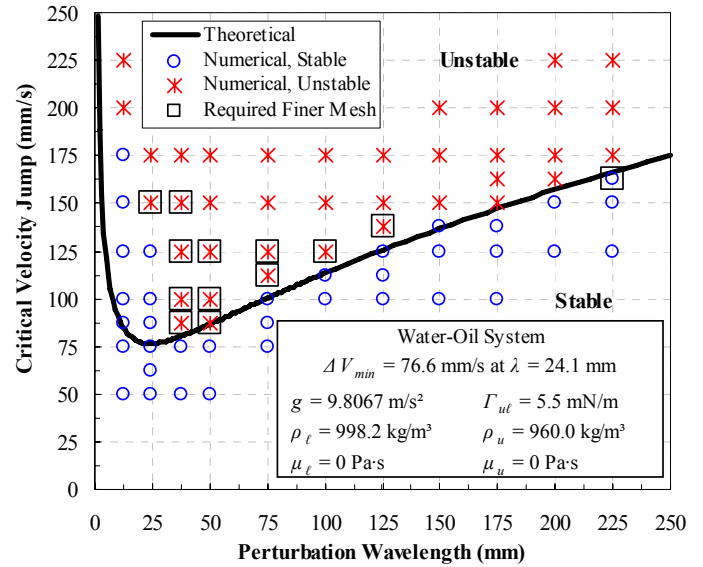


Figure 19. Kelvin-Helmholtz Instability Model Validation

Certain cases, highlighted in Figure 19, did not exhibit the expected behavior with the 2.5-mm square mesh, which was corrected by using the 1-mm square mesh. Using a mesh with very small elements at the interface that grew larger with distance from the interface did not alleviate the problem because of the aspect ratio of the elements. To successfully simulate the Kelvin-Helmholtz instability phenomenon required both small cells and well-shaped cells (to capture the high vorticity in this problem). Some cases that were expected to result in an unstable interface did not produce any billows, so further investigation is required. Nevertheless, Figure 19 shows that it is possible to model the instability phenomena as well as to reproduce accurately most of the neutral stability curve.

Substituting steel and slag properties into the Kelvin-Helmholtz equation studied here yields critical surface velocities around 0.4 m/s. This is typical of estimates based on plant measurements discussed earlier¹⁴. The modeling tool developed in this work can be used to include more realistic casting conditions, in order to validate and extend Equations (17) or (18) to steel casting conditions.

CONCLUSIONS

Many studies have been performed over the years to investigate mold slag entrainment, which is one of the main sources of inclusion defects in continuous casting of steel. This work identifies nine distinct mechanisms responsible for entrainment, especially vortexing due to asymmetric flow, argon bubble interactions with the slag layer, shear-layer instability at the slag-steel interface, and excessive upward flow impingement on the meniscus. Other important mechanisms include meniscus level fluctuations, meniscus freezing and hook formation, and meniscus balding. Standing wave instability appears unlikely as shear-layer instability can occur more easily. The slag layer can also crawl down the SEN, but this effect is only likely at very shallow submergence depths, or with slag foaming. The various simple models available to estimate these nine mechanisms are summarized here. They can be used together to evaluate flow patterns in physical or numerical models of the flow field in the molten steel pool. The shear-layer instability phenomena was explored further in this work with a numerical model, which was proven to match the analytical predictions. However, more work is required, for this mechanism and others, owing to limited understanding of the nature of entrainment mechanisms, and for the simple fact that water-oil systems behave differently than steel-slag systems.

ACKNOWLEDGEMENTS

The authors gratefully acknowledge the financial support of the member companies of the Continuous Casting Consortium at the University of Illinois, as well as the computational resources provided by The National Center for Supercomputing Applications (NCSA) at the University of Illinois. The authors thank Professor S. P. Vanka and Rajneesh Chaudhary for enlightening discussions on the numerical modeling aspects of this paper, and Junya Iwasaki for assistance with translation of some of the references.

REFERENCES

1. R. Chaudhary, B.T. Rietow, and B.G. Thomas, "Differences between Physical Water Models and Steel Continuous Casters: A Theoretical Evaluation", *Proceedings of the 2009 Materials Science and Technology Conference, AIST/TMS*, (2009), pg. 1090-1101.

2. J. Herbertson, Q.L. He, P.J. Flint, and R.B. Mahapatra, "Modelling of Metals Delivery to Continuous Casting Moulds." *Steelmaking Conference Proceedings*, The Iron and Steel Society, **74** (1991), pg. 171-185.
3. M. Suzuki, M. Suzuki, and M. Nakada, "Perspectives of Research on High-Speed Conventional Slab Continuous Casting of Carbon Steels." *ISIJ International* **41**:7 (2001), pg. 670-682.
4. B.G. Thomas "Modeling of Continuous-Casting Defects Related to Mold Fluid Flow." *Proceedings of the International Congress on the Science and Technology of Steelmaking*, The Association for Iron and Steel Technology, **3** (2005), pg. 847-861.
5. Q. Yuan and B.G. Thomas, "Transport and Entrapment of Particles in Continuous Casting of Steel." *Proceedings of Modeling of Casting, Welding, and Advanced Solidification Processes*, The Minerals, Metals, and Materials Society, **11** (2006), pg. 745-752.
6. G.-G. Lee, H.-J. Shin, B.G. Thomas, and S.-H. Kim, "Asymmetric Multi-Phase Fluid Flow and Particle Entrapment in a Continuous Casting Mold." *Proceedings of AISTech 2008*, (2008), No. 2, pg. 63-73.
7. S. Kunstreich and P.H. Dauby, "Effect of Liquid Steel Flow Pattern on Slab Quality and the Need for Dynamic Electromagnetic Control in the Mould." *Ironmaking and Steelmaking* **32**:1 (2005), pg. 80-86.
8. A.W. Cramb, Y. Chung, J. Harman, A. Sharan, and I. Jimbo, "The Slag/Metal Interface and Associated Phenomena." *Iron and Steelmaker* **24**:3 (1997), pg. 77-83.
9. D. Bouris and G. Bergeles, "Investigation of Inclusion Re-Entrainment from the Steel-Slag Interface." *Metallurgical and Materials Transactions* **29B**:3 (1998), pg. 641-649.
10. J. Strandh, K. Nakajima, R. Eriksson, and P. Jönsson, "A Mathematical Model to Study Liquid Inclusion Behavior at the Steel-Slag Interface." *ISIJ International* **45**:12 (2005), pg. 1838-1847.
11. C. Ojeda, B.G. Thomas, J. Barco, and J.L. Arena, "Model of Thermal-Fluid Flow in the Meniscus Region During an Oscillation Cycle." *Proceedings of AISTech 2007*, (2007), No. 2, pg. 269-283.
12. J. Sengupta, C. Ojeda, and B. G. Thomas, "Thermal-Mechanical Behaviour during Initial Solidification in Continuous Casting: Steel Grade Effects." *International Journal of Cast Metals Research* **22**:1-4 (2009), pg. 8-14.
13. T. Teshima, M. Osame, K. Okimoto, and Y. Nimura, "Improvement of Surface Property of Steel at High Casting Speed." *Steelmaking Conference Proceedings*, The Iron and Steel Society, **71** (1988), pg. 111-118.
14. J. Kubota, K. Okimoto, A. Shirayama, and H. Murakami, "Meniscus Flow Control in the Mold by Travelling Magnetic Field for High Speed Slab Caster." *Steelmaking Conference Proceedings*, The Iron and Steel Society, **74** (1991), pg. 233-241.
15. H. Nakato, K. Saito, Y. Oguchi, N. Namura, and K. Sorimachi, "Surface Quality Improvement of Continuously Cast Blooms by Optimizing Solidification in Early Stage." *Steelmaking Conference Proceedings*, The Iron and Steel Society, **70** (1987), pg. 427-431.
16. Z. Wang, K. Mukai, Z. Ma, M. Nishi, H. Tsukamoto, and F. Shi, "Influence of Injected Ar Gas on the Involvement of the Mold Powder Under Different Wettabilities Between Porous Refractory and Molten Steel." *ISIJ International* **39**:8 (1999), pg. 795-803.
17. P. Andrzejewski, K.-U. Köhler, and W. Pluschkell, "Model Investigations on the Fluid Flow in Continuous Casting Moulds of Wide Dimensions." *Steel Research International* **63**:6 (1992), pg. 242-246.
18. Y.H. Wang, "A Study of the Effect of Casting Conditions on Fluid Flow in the Mold Using Water Modelling." *Steelmaking Conference Proceedings*, The Iron and Steel Society, **73** (1990), pg. 473-480.
19. Q. He, G. Evans, R. Serje, and T. Jaques, "Fluid Flow and Mold Slag Entrainment in the Continuous Twin-Slab Casting Mould." *Proceedings of AISTech 2009*, (2009), No. 2, pg. 573-588.
20. K. Cukierski and B.G. Thomas, "Flow Control with Local Electromagnetic Braking in Continuous Casting of Steel Slabs." *Metallurgical and Materials Transactions* **39B**:1 (2008), pg. 94-107.
21. A. Matsushita, K. Isogami, M. Temma, T. Ninomiya, and K. Tsutsumi, "Direct Observation of Molten Steel Meniscus in CC Mold during Casting." *Transactions of the ISIJ* **28**:7 (1988), pg. 531-534.
22. B.S. Moghaddam, E. Steinmetz, P. R. Scheller, "Interaction Between the Flow Condition and the Meniscus Disturbance in the Continuous Slab Caster." *Proceedings of the International Congress on the Science and Technology of Steelmaking*, The Association for Iron and Steel Technology, **3** (2005), pg. 911-920.
23. G.A. Panaras, A. Theodorakakos, and G. Bergeles, "Numerical Investigation of the Free Surface in a Continuous Steel Casting Mold." *Metallurgical and Materials Transactions* **29B**:5 (1998), pg. 1117-1126.
24. M. Javurek, M. Thumfart, K. Rieger, M. Hirschmanner, "Mathematical Mould Level Model Based on Numerical Simulations and Water Model Experiments." *Proceedings of the 6th European Conference on Continuous Casting*, (2008).
25. T. Honeyands and J. Herbertson, "Flow Dynamics in Thin Slab Caster Moulds." *Steel Research International* **66**:7 (1995), pg. 287-293.
26. H. Nakamura, S. Kohira, J. Kubota, T. Kondo, M. Suzuki, and Y. Shiratani, "Technology for Production of High Quality Slab at High Speed Casting." *Steelmaking Conference Proceedings*, The Iron and Steel Society, **75** (1992), pg. 409-415.
27. H. Yuyama, *et al.*, "Development of Bath Level Variation Detector in CC Mold." *Tetsu-to-Hagane* **72**:12 (1986), pg. S1018.
28. J. Sengupta, B.G. Thomas, H.-J. Shin, G.-G. Lee, and S.-H. Kim, "A New Mechanism of Hook Formation during Continuous Casting of Ultra-Low-Carbon Steel Slabs." *Metallurgical and Materials Transactions* **37A**:5 (2006), pg. 1597-1611.
29. G.-G. Lee, B.G. Thomas, S.-H. Kim, H.-J. Shin, S.-K. Baek, C.-H. Choi, D.-S. Kim, and S.-J. Yu, "Microstructure Near Corners of Continuous-Cast Steel Slabs Showing Three-Dimensional Frozen Meniscus at Hooks." *Acta Materialia* **55**:20 (2007), pg. 6705-6712.

30. W.H. Emling, T.A. Waugaman, S.L. Feldbauer, and A.W. Cramb, "Subsurface Mold Slag Entrainment in Ultra Low Carbon Steels." *Steelmaking Conference Proceedings*, The Iron and Steel Society, **77** (1994), pg. 371-379.
31. J. Knoepke, M. Hubbard, J. Kelly, R. Kittridge, and J. Lucas, "Pencil Blister Reduction at Inland Steel Company." *Steelmaking Conference Proceedings*, The Iron and Steel Society, **77** (1994), pg. 381-388.
32. S. Yamashita and M. Iguchi, "Mechanism of Mold Powder Entrapment Caused by Large Argon Bubble in Continuous Casting Mold." *ISIJ International* **41**:12 (2001), pg. 1529-1531.
33. T. Watanabe and M. Iguchi, "Water Model Experiments on the Effect of an Argon Bubble on the Meniscus Near the Immersion Nozzle." *ISIJ International* **49**:2 (2009), pg. 182-188.
34. R.M. McDavid and B.G. Thomas, "Flow and Thermal Behavior of the Top Surface Flux/Powder Layers in Continuous Casting Molds." *Metallurgical and Materials Transactions* **27B**:4 (1996), pg. 672-685.
35. B. Zhao, S.P. Vanka, and B.G. Thomas, "Numerical Study of Flow and Heat Transfer in a Molten Flux Layer." *International Journal of Heat and Fluid Flow* **26**:1 (2005), pg. 105-118.
36. H. Bai and B.G. Thomas, "Effects of Clogging, Argon Injection, and Continuous Casting Conditions on Flow and Air Aspiration in Submerged Entry Nozzles." *Metallurgical and Materials Transactions* **32B**:4 (2001), pg. 707-722.
37. S. Mahmood, "Efficient Modeling of Flow Asymmetries and Particle Entrapment in Nozzle and Mold During Continuous Casting of Steel Slabs." Masters Thesis, The University of Illinois at Urbana-Champaign, (2006).
38. L. Zhang, Y. Wang, and X. Zuo, "Flow Transport and Inclusion Motion in Steel Continuous-Casting Mold under Submerged Entry Nozzle Clogging Condition." *Metallurgical and Materials Transactions* **39B**:4 (2008), pg. 534-550.
39. H. Bai and B.G. Thomas, "Turbulent Flow of Liquid Steel and Argon Bubbles in Slide-Gate Tundish Nozzles: Part I. Model Development and Validation." *Metallurgical and Materials Transactions* **32B**:2 (2001), pg. 253-267.
40. H. Bai and B.G. Thomas, "Turbulent Flow of Liquid Steel and Argon Bubbles in Slide-Gate Tundish Nozzles: Part II. Effect of Operation Conditions and Nozzles Design." *Metallurgical and Materials Transactions* **32B**:2 (2001), pg. 269-284.
41. S.-M. Cho, G.-G. Lee, S.-H. Kim, R. Chaudhary, O.-D. Kwon, and B.G. Thomas, "Effect of Stopper-Rod Misalignment on Asymmetric Flow and Vortex Formation in Steel Slab Casting." *Jim Evans Honorary Symposium, in Proceedings of The Minerals, Metals, and Materials Society Annual Meeting 2009*, The Minerals, Metals, and Materials Society, **139** (2009), pg. 71-77.
42. J. Yoshida, T. Ohmi, and M. Iguchi, "Cold Model Study on the Effects of Density Difference and Blockage Factor on Mold Powder Entrainment." *ISIJ International* **45**:8 (2005), pg. 1160-1164.
43. Y. Ueda, T. Kida, and M. Iguchi, "Unsteady Pressure Coefficient Around an Elliptic Immersion Nozzle." *ISIJ International* **44**:8 (2004), pg. 1403-1409.
44. B. Li, T. Okane, and T. Umeda, "Modeling of Biased Flow Phenomena Associated with the Effects of Static Magnetic-Field Application and Argon Gas Injection in Slab Continuous Casting of Steel." *Metallurgical and Materials Transactions* **32B**:6 (2001), pg. 1053-1066.
45. B. Li and F. Tsukihashi, "Vortexing Flow Patterns in a Water Model of Slab Continuous Casting Mold." *ISIJ International* **45**:1 (2005), pg. 30-36.
46. N. Kasai and M. Iguchi, "Water-Model Experiment on Melting Powder Trapping by Vortex in the Continuous Casting Mold." *ISIJ International* **47**:7 (2007), pg. 982-987.
47. Q. He, "Observations of Vortex Formation in the Mould of a Continuous Slab Caster." *ISIJ International* **33**:2 (1993), pg. 343-345.
48. M. Gebhard, Q.L. He, and J. Herbertson, "Vortexing Phenomena in Continuous Slab Casting Moulds." *Steelmaking Conference Proceedings*, The Iron and Steel Society, **76** (1993), pg. 441-446.
49. D. Gupta and A.K. Lahiri, "Water-Modeling Study of the Surface Disturbances in Continuous Slab Caster." *Metallurgical and Materials Transactions* **25B**:2 (1994), pg. 227-233.
50. B. Li and F. Tsukihashi, "Effects of Electromagnetic Brake on Vortex Flows in This Slab Continuous Casting Mold." *ISIJ International* **46**:12 (2006), pg. 1833-1838.
51. G. Kastner, W. Brandstätter, B. Kaufmann, C. Wassermayr, and M. Javurek, "Numerical Study on Mould Powder Entrapment Caused by Vortexing in a Continuous Casting Process." *Steel Research International* **77**:6 (2006), pg. 404-408.
52. D. Gupta and A.K. Lahiri, "Cold Model Study of Slag Entrainment into Liquid Steel in Continuous Slab Caster." *Ironmaking and Steelmaking* **23**:4 (1996), pg. 361-363.
53. K. Tsutsumi, K. Watanabe, M. Suzuki, M. Nakada, and T. Shiomi, "Effect of Properties of Mold Powder Entrapped in Molten Steel in a Continuous Casting Process." *VII International Conference on Molten Slags, Fluxes, and Salts*, The South African Institute of Mining and Metallurgy, (2004), pg. 803-806.
54. J.W. Rottman, "Steep Standing Waves at a Fluid Interface." *Journal of Fluid Mechanics* **124** (1982), pg. 283-306.
55. A. Theodorakakos and G. Bergeles, "Numerical Investigation of the Interface in a Continuous Steel Casting Mold Water Model." *Metallurgical and Materials Transactions* **29B**:6 (1998), pg. 1321-1327.
56. J. Anagnostopoulos and G. Bergeles, "Three-Dimensional Modeling of the Flow and the Interface Surface in a Continuous Casting Mold Model." *Metallurgical and Materials Transactions* **30B**:6 (1999), pg. 1095-1105.
57. D. Gupta and A.K. Lahiri, "Water Modelling Study of the Jet Characteristics in a Continuous Casting Mould." *Steel Research International* **63**:5 (1992), pg. 201-204.

58. F.M. Najjar, B.G. Thomas, and D.E. Hershey, "Numerical Study of Steady Turbulent Flow through Bifurcated Nozzles in Continuous Casting." *Metallurgical and Materials Transactions* **26B**:4 (1995), pg. 749-765.
59. D. Gupta and A.K. Lahiri, "Cold Model Study of the Surface Profile in a Continuous Slab Casting Mold: Effect of Second Phase." *Metallurgical and Materials Transactions* **27B**:4 (1996), pg. 695-697.
60. M. Kamal and Y. Sahai, "Modeling of Melt Flow and Surface Standing Waves in a Continuous Casting Mold." *Steel Research International* **76**:1 (2005), pg. 44-52.
61. S.K. Dash, S.S. Mondal, and S.K. Ajmani, "Mathematical Simulation of Surface Wave Created in a Mold Due to Submerged Entry Nozzle." *International Journal of Numerical Methods for Heat and Fluid Flow* **14**:5 (2004), pg. 606-632.
62. B. Rietow, "Fluid Velocity Simulation and Measurement in Thin Slab Casting." Masters Thesis, The University of Illinois at Urbana-Champaign, (2007).
63. H.L.F. von Helmholtz, "Über discontinuierliche Fließbewegungen." *Monatsberichte der Königlich Preussischen Akademie der Wissenschaften zu Berlin* **23** (1868), pg. 215-228.
64. W. Thomson (Lord Kelvin), "Hydrokinetic Solutions and Observations." *Philosophical Magazine* **42**:281 (1871), pg. 362-377.
65. S. Chandrasekhar, *Hydrodynamic and Hydromagnetic Stability*. Clarendon Press, Oxford, (1961), pg. 481-514.
66. P. Cha and J. Yoon, "The Effect of a Uniform Direct Current Magnetic Field on the Stability of a Stratified Liquid Flux/Molten Steel System." *Metallurgical and Materials Transactions* **31B**:2 (2000), pg. 317-326.
67. T. Funada and D.D. Joseph, "Viscous Potential Flow Analysis of Kelvin-Helmholtz Instability in a Channel." *Journal of Fluid Mechanics* **445** (2001), pg. 263-283.
68. L.M. Milne-Thomson, *Theoretical Hydrodynamics*, 5e. Macmillan Press, London, (1968).
69. M. Iguchi, J. Yoshida, T. Shimizu, and Y. Mizuno, "Model Study on the Entrapment of Mold Powder into Molten Steel." *ISIJ International* **40**:7 (2000), pg. 685-691.
70. J.M. Harman and A.W. Cramb, "A Study of the Effect of Fluid Physical Properties upon Droplet Emulsification." *Steelmaking Conference Proceedings*, The Iron and Steel Society, **79** (1996), pg. 773-784.
71. J. Savolainen, T. Fabritius, and O. Mattila, "Effect of Fluid Physical Properties on the Emulsification." *ISIJ International* **48**:1 (2009), pg. 29-36.
72. Z. Xiao, Y. Peng, and C. Liu, "Modelling Study of the Entrapment Phenomena at the Slag-Metal Interface in the Gas-Stirred Ladle." *Chinese Journal of Metal Science and Technology* **3** (1987), pg. 187-193.
73. T. Wei and F. Oeters, "A Model Test for Emulsion in Gas-Stirred Ladles." *Steel Research International* **63**:2 (1992), pg. 60-68.
74. K. Krishnapisharody and G.A. Irons, "Model Studies on Slag Droplet Generation in Gas-Stirred Ladles." *EPD Congress 2008, in Proceedings of The Minerals, Metals, and Materials Society Annual Meeting 2008*, The Minerals, Metals, and Materials Society, **138** (2008), pg. 293-302.
75. K. Krishnapisharody and G.A. Irons, "Numerical Simulation of Droplet Generation of the Buoyant Phase in Two-Phase Liquid Baths." *EPD Congress 2008, in Proceedings of The Minerals, Metals, and Materials Society Annual Meeting 2008*, The Minerals, Metals, and Materials Society, **138** (2008), pg. 311-322.
76. K. Krishnapisharody and G. A. Irons, "Modeling and Analysis of Slag Droplet Formation in Ladle Metallurgy Practice." *Proceedings of AISTech 2008*, (2008), No. 2, pg. 1243-1252.
77. D.J. Harris and J.D. Young, "Water Modeling – A Viable Production Tool." *Steelmaking Conference Proceedings*, The Iron and Steel Society, **65** (1982), pg. 3-16.
78. FLUENT 6.3 User Manuals, Fluent, Inc. (2007), Lebanon, NH, USA.
79. J.A. Dantzig and C.L. Tucker III, *Modeling in Materials Processing*. Cambridge University Press, Cambridge, (2001), pg. 24-59 and 149-157.
80. C.W. Hirt and B.D. Nichols, "Volume of Fluid (VOF) Method for the Dynamics of Free Boundaries." *Journal of Computational Physics* **39**:1 (1981), pg. 201-225.
81. S. Muzaferija, M. Peric, P. Sames, and T. Schellin, "A Two-Fluid Navier-Stokes Solver to Simulate Water Entry." *Proceedings of the 22nd Symposium on Naval Hydrodynamics*, (1999), pg. 638-649.
82. J.U. Brackbill, D.B. Kothe, and C. Zemach, "A Continuum Method for Modeling Surface Tension." *Journal of Computational Physics* **100**:2 (1992), pg. 335-354.
83. R.I. Issa, "Solution of the Implicitly Discretised Fluid Flow Equations by Operator-Splitting." *Journal of Computational Physics* **62**:1 (1985), pg. 40-65.